Springer

KSME

Journal of Mechanical Science and Technology 29 (9) (2015) 3707~3716
www.springerlink.com/content/1738-494x(Print)/1976-3824(Online)
DOI 10.1007/s12206-015-0816-4

Numerical investigation of cavitation-vortex interaction in a mixed-flow waterjet pump †

Renfang Huang[1], Bin Ji[2], Xianwu Luo[1,*], Zhihong Zhai[3] and Jiajian Zhou[3]

[1]*State Key Laboratory of Hydroscience and Engineering, Tsinghua University, Beijing, 100084, China*
[2]*School of Power and Mechanical Engineering, Wuhan University, Hubei, 430072, China*
[3]*Marine Design and Research Institute of China, Shanghai, 200000, China*

(Manuscript Received January 31, 2015; Revised April 16, 2015; Accepted April 21, 2015)

Abstract

Turbulent cavitating flows in a mixed-flow waterjet pump were numerically investigated using the k-ω SST turbulence model and the mass transfer cavitation model based on the Rayleigh-Plesset equation to provide a comprehensive understanding of the cavitation-vortex interaction mechanism. The predicted hydraulic performance, as well as the cavitation performance, exhibits a reasonable agreement with the experimental results. The vorticity distributions under three operation conditions were illustrated together. Based on the illustration, cavitation development enhances vorticity production and flow unsteadiness in a mixed-flow waterjet pump. Vortices are basically located at the cavity interface, particularly at the downstream interface, during cavitation. Further analyses using the relative vorticity transport equation in cavitating turbulent flows indicate that vortex dilation and baroclinic torque exhibit a steep jump as cavitation occurs. In addition, vortex stretching contributes mainly to large-scale vortex generation.

Keywords: Cavitation; Mixed-flow pump; Numerical simulation; Vortex; Waterjet pump

1. Introduction

Propellers have played a dominant role in marine propulsion; however, they exhibit numerous drawbacks in large and high-speed vessels. These drawbacks include hydrodynamic-excited noise, vibration, and erosion. By contrast, waterjet pumps, which utilize counterforce to propel vessels with a closed flow passage, have received increasing attention as a potential propulsion method in high-performance vessels.

In the past, investigations on waterjet pumps focused on performance prediction and design optimization. Oh et al. [1-3] applied the conceptual method to design a mixed-flow marine pump and investigated the effects of blade stacking on cavitation performance. Bonaiuti et al. [4] studied parameter effects, including impeller blade loading, stacking, exit vortex distribution, leading edge sweep angle, and exit hub radius. They obtained an optimal configuration by considering suction performance and hydrodynamic efficiency.

With regard to high rotational speed, cavitation is inevitable in a waterjet pump and will lead to unfavorable results, such as head and efficiency drop, noise, and vibration [5, 6]. Thus, numerous studies have been conducted to predict cavitating flows accurately by focusing on various research objects such as Francis turbines [7], hydrofoils [8], centrifugal pumps [9, 10], cryogenic fluids [11], marine propellers [12, 13], and waterjet propulsors [14-17]. Rhee et al. [18] found that cavitation inception and cavity shape in a marine propeller could be predicted well using an unstructured grid, which demonstrated the feasibility of cavitation simulation based on Reynolds-averaged Navier-Stokes (RANS) method.

However, most studies have investigated the performance breakdown and structures of cavitating flows, and only a few have illustrated the interaction between cavitation and vortices. In fact, cavitating vortical structures can be found in various types of hydraulic machineries and will primarily affect cavitation inception in numerous turbulent flows [19, 20]. Therefore, revealing cavitation-vortex interaction and the mechanism of vorticity evolutions in cavitating flows is urgently required.

The present study investigated cavitating turbulent flows in a mixed-flow waterjet pump using the k-ω SST turbulence model and the mass transfer cavitation model based on the Rayleigh-Plesset equation. Cavitation evolution at three typical span surfaces was discussed by emphasizing cavitation-vortex interaction using the relative vorticity transport equation.

*Corresponding author. Tel.: +86 10 62789853, Fax.: +86 10 62789853
E-mail address: luoxw@tsinghua.edu.cn; hrenfang@yeah.net
† Recommended by Associate Editor Shin Hyung Rhee

Table 1. Geometric parameters of the mixed-flow waterjet pump.

Parameters	Symbols	Values
Blade width ratio at the inlet	b_1/D_2	0.318
Blade width ratio at the exit	b_2/D_2	0.247
Blade inlet diameter at the tip	D_{1t}/D_2	0.856
Blade inlet diameter at the hub	D_{1h}/D_2	0.245

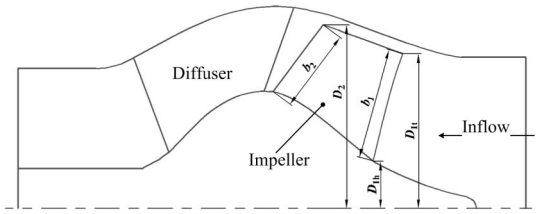

(a) Meridional passage

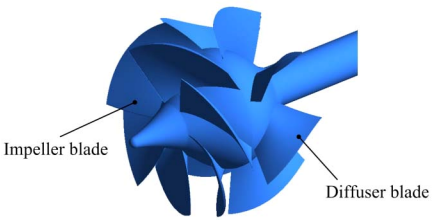

(b) 3D view of the waterjet pump

Fig. 1. Geometry of the mixed-flow waterjet pump.

2. Pump configuration and mesh generation

2.1 Pump geometry

The mixed-flow waterjet pump used in the present research is composed of a six-blade impeller, a seven-blade diffuser, a suction pipe, and an outlet pipe with a clearance of 0.3 mm between the impeller blade tip and the pump casing , as shown in Fig. 1. Its design operation point is a flow discharge of Q = 0.445 m^3/s and a rotational speed of n = 1450 r/min.

The main geometric parameters of the mixed-flow waterjet pump are listed in Table 1. D_2 is the blade tip diameter with a value of 345 mm and b_2 is the blade width at the impeller outlet. D_{1t} and D_{1h} correspond to the blade tip and hub diameter at the impeller inlet, respectively. Lastly, b_1 is the blade width at the impeller inlet.

2.2 Structured mesh generation

A full flow passage from the inlet pipe to the outlet pipe was considered as the computational domain in the present study, with the structural grids generated in the commercial software ICEM CFD. O-H type grids were produced in the impeller and diffuser with sufficient refinement made around the blade surfaces to satisfy the requirement of the turbulence model.

Mesh influence was investigated by monitoring the hydraulic efficiency of the waterjet pump. The present study focused on cavitation-vortex interaction in the impeller; hence, six mesh resolutions with the same topology were tested, as illustrated in Fig. 2. The only difference was the number of nodes distributed along various topology sides, as presented in Figs. 2(b)-2(d). For each mesh resolution, 25 layers were cut to make the fine mesh in the blade tip clearance area, as shown in Fig. 2(e). The results showed that hydraulic efficiency remained stable (i.e., fluctuation stayed within 0.05%) after the domain mesh nodes reached 106×10^4. Thus, the mesh resolution of 106×10^4 nodes was selected for the final mesh.

Moreover, grid quality was evaluated by the determinant 2×2×2 (≥ 0.395 in the impeller and ≥ 0.584 in the diffuser) with the mesh refined around the surfaces of the impeller blades ($4 < y+ < 90$), as shown in Fig. 3. This figure demonstrates that the generated structured mesh is suitable to capture the detailed structures of cavities and vortices.

3. Numerical methods

3.1 Governing equations

Cavitating turbulent flows were solved based on the homogenous assumption that the multiphase flows of liquid and vapor fluids were considered one, and thus, they shared the same velocity and pressure. The continuity and momentum equations, i.e., RANS equations, are as follows:

$$\frac{\partial \rho_m}{\partial t}+\frac{\partial}{\partial x_j}\left(\rho_m u_j\right)=0\,, \tag{1}$$

$$\frac{\partial}{\partial t}\left(\rho_m u_i\right)+\frac{\partial}{\partial x_j}\left(\rho_m u_i u_j\right)=-\frac{\partial p}{\partial x_i}+\frac{\partial}{\partial x_j}\left[\left(\mu+\mu_t\right)\left(\frac{\partial u_i}{\partial x_j}+\frac{\partial u_j}{\partial x_i}-\frac{2}{3}\frac{\partial u_k}{\partial x_k}\delta_{ij}\right)\right], \tag{2}$$

where p is the mixture pressure, u_i is the velocity in the i direction, μ is the laminar viscosity, and μ_t is the turbulent eddy viscosity. The mixture density ρ_m is defined as follows:

$$\rho_m=\alpha_v\rho_v+\left(1-\alpha_v\right)\rho_l\,, \tag{3}$$

where subscripts v and l represent the vapor and liquid phase, respectively; and α_v is denoted as the vapor volume fraction.

In the present study, the k-ω SST turbulence model is used to close the RANS equations to realize its advantage over accurate predictions of flow separation under adverse pressure gradients given that turbulent shear stress transportation is considered and its impressive prediction performance has been demonstrated in validation studies [21].

3.2 Cavitation model

To make the vapor volume fraction conservative, the cavitation model was derived from the mass transfer equation as follows:

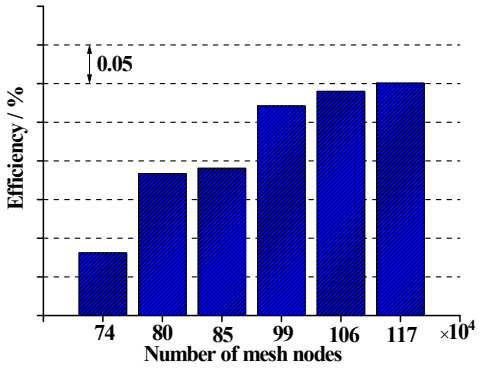

(a)

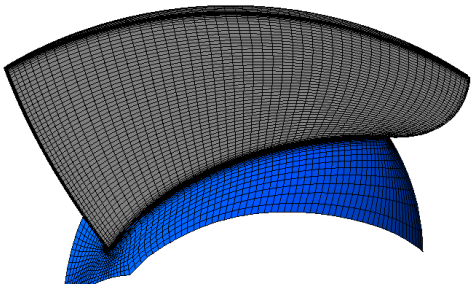

(b) Mesh case of 74×10^4 nodes

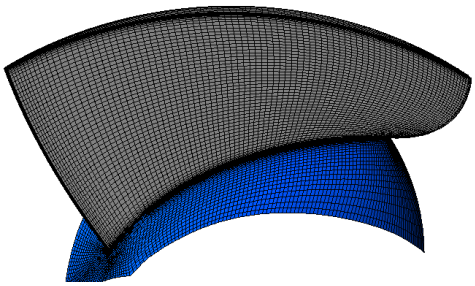

(c) Mesh case of 106×10^4 nodes

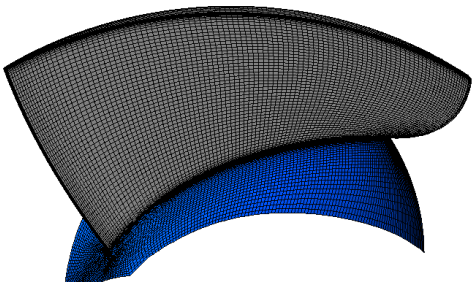

(d) Mesh case of 117×10^4 nodes

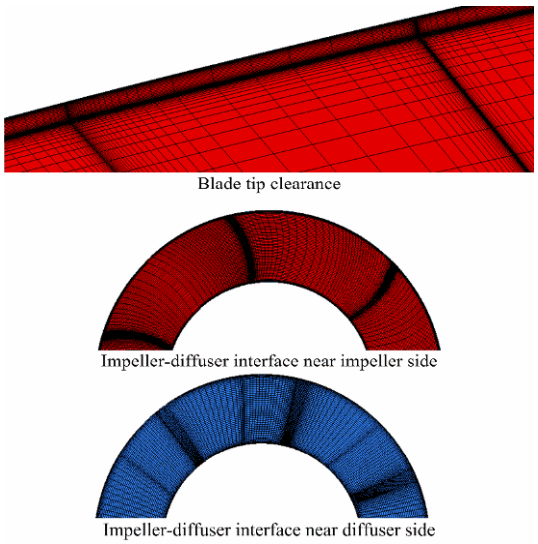

(e) Mesh detailed distribution with 106×10^4 nodes

Fig. 2. Mesh independence test results and mesh distributions.

$$\frac{\partial \rho_v \alpha_v}{\partial t} + \nabla \bullet \left(\rho_v \alpha_v u_i \right) = \dot{m}^+ - \dot{m}^- . \tag{4}$$

The source terms that correspond to the vaporization term (i.e., $\dot{m}^+$) and condensation term (i.e., $\dot{m}^-$) are given by Zwart et al. [22]:

$$\dot{m}^+ = F_{vap} \frac{3 r_{nuc} \left(1-\alpha_v\right) \rho_v}{R_{nuc}} \sqrt{\frac{2}{3} \frac{\max\left(p_v - p, 0\right)}{\rho_l}} , \tag{5}$$

$$\dot{m}^- = F_{cond} \frac{3 \alpha_v \rho_v}{R_{nuc}} \sqrt{\frac{2}{3} \frac{\max\left(p - p_v, 0\right)}{\rho_l}} , \tag{6}$$

where F_{vap} and F_{cond} are the empirical coefficients for the mass transfer process with recommended values of 50 and 0.01, respectively [22]. r_{nuc} is the nucleation volume fraction with the value of 5×10^{-4}. R_{nuc} is the bubble radius with the value of 1×10^{-6} m. These parameters of the cavitation model were discussed and validated based on experimental data [22] with

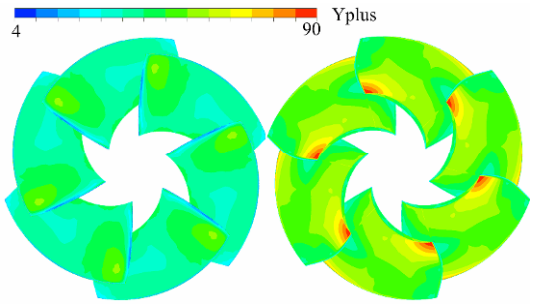

(a) Suction surface (b) Pressure surface

Fig. 3. Yplus distribution in the impeller.

successful simulations of cavitating flows in pumps [6].

3.3 Boundary conditions

In this section, 3D cavitating turbulent flows in the mixed-flow waterjet pump were calculated using the commercial software ANSYS CFX 14.0. Water at 25°C was used as the liquid in the simulation, whose density was 997 kg/m^3 and dynamic viscosity was 8.899×10^{-4} kg·m^{-1}·s^{-1}. Water vapor at 25°C with a density of 0.02308 kg/m^3 and a dynamic viscosity of 9.8626×10^{-6} kg·m^{-1}·s^{-1} was used as the vaporized fluid when cavitation occurred. The convergence residual was set at less than 1×10^{-5}. Hydraulic head and efficiency were monitored to reach an unaltered value.

For the boundary conditions, the total pressure was set at the computational domain inlet plane and gradually reduced when cavitation was considered. Mass flow discharge was assigned at the outflow plane based on the operation condition. Given that the impeller domain was rotating while the inlet pipe, diffuser, and outlet pipe were set as stationary assemblies in the absolute reference frame, two frozen rotor interfaces were assigned between the rotating and stationary frames. A non-slip wall was specified at all flow passage walls. A high resolution scheme was set for the advection term.

4. Results and discussions

4.1 Pump performance

Experimental tests were conducted in the laboratory of the Marine Design and Research Institute of China. Flow rates were measured by an electromagnetic flow meter, input power was acquired by a torque transducer, and pump head was derived from the total pressure difference between the inlet and outlet pipes.

Non-dimensional parameters are specified in Table 2 to express pump performance clearly. Moreover, cavitation characteristics were described by the available net positive suction head ($NPSH_A$), the definition of which is given in Eq. (7). Subsequently, the Thoma's cavitation number σ is calculated using Eq. (8).

Table 2. Non-dimensional parameters for pump performance.

Definition	Symbol	Expression
Flow coefficient	ϕ	$\frac{Q}{\pi D_2 b_2 u_2}$
Head coefficient	Ψ	$\frac{H}{u_2^2/2g}$
Hydraulic efficiency	η	$\frac{\rho_l g Q H}{M\omega}$

$$NPSH_A=\left(\frac{p_{in}}{\rho g}+\frac{v_{in}^2}{2g}\right)-\frac{p_v}{\rho g}, \tag{7}$$

where p_{in} and v_{in} are the static pressure and velocity at the inlet plane, respectively; p_v is the saturation vapor pressure of water at room temperature; and g is gravity acceleration.

$$\sigma=\frac{NPSH_A}{H}, \tag{8}$$

where H is the pump head.

In Table 2, Q is the flow rate of the waterjet pump; M is the torque input to the pump shaft; ω is the rotational angular velocity, which is equal to $2\pi n/60$; and u_2 is the peripheral velocity at the exit of the blade tip, which is equal to $\omega D_2/2$.

The experimental characteristic curves (marked as "exp.") and calculation data (marked as "cal.") are presented in Fig. 4. The calculated head coefficients agree well with the experimental results, and the predicted efficiency curve exhibits the same tendency as the experimental curve. The predicted efficiency was reasonably larger than the tested efficiency because the mechanical loss of the pump was not considered.

The decrease in performance during cavitation development under the design operation condition is illustrated in Fig. 5. As shown in the figure, head coefficient and efficiency decreased at low cavitation numbers. The effects of cavitation on pump performance were reasonably predicted by the present simulation even though critical cavitation numbers, wherein pump performance suddenly broke down, were different between the calculation and the experiment. Such discrepancy could be attributed to the limitation of the cavitation model based on the homogeneous flow assumption that water and vapor had the same velocity and pressure distributions. Although the empirical coefficients in the adopted model have been validated by experimental data [22], optimal coefficients for specific problems remain [23]. Moreover, many factors were not included in the cavitation model, such as turbulence effects, surface tension, and viscosity.

In addition, the turbulence model should be responsible for the discrepancy in cavitation prediction because turbulence eddy viscosity was overpredicted by the conventional turbulence model in cavitating regions [24]. Consequently, cavitation effect was underestimated and reentrant flows were pre-

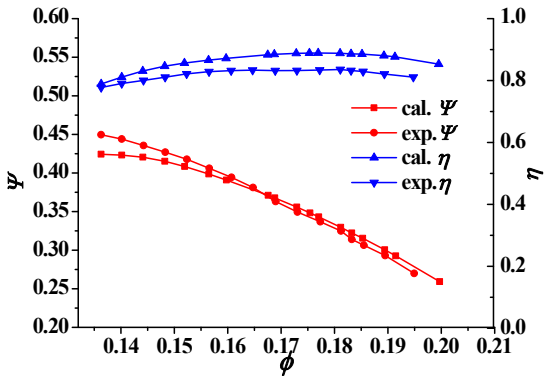

Fig. 4. Characteristic curves of the mixed-flow waterjet pump.

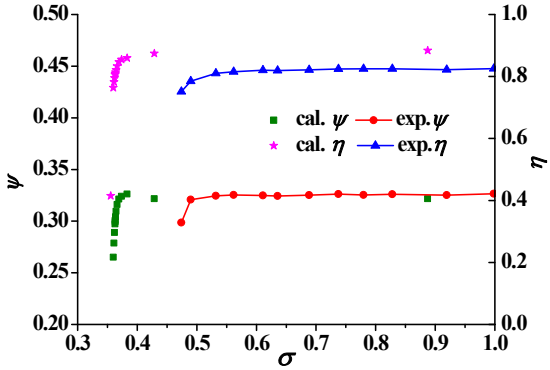

Fig. 5. Cavitation performance curves at the design operation point.

maturely stopped to reduce sheet cavitation. Hence, the predicted cavitation performance is better than its experimental counterpart, as shown in Fig. 5.

4.2 Vortex analysis

In this study, the relative transport equation, that is, Eq. (9), was used to analyze cavitating turbulent flows in the mixed-flow waterjet pump to improve understanding of the mechanism of cavitation-vortex interaction.

$$\frac{\mathrm{D}\Omega_\mathrm{r}}{\mathrm{D}t}=\left(\Omega_\mathrm{r}\bullet\nabla\right)\vec{W}-\Omega_\mathrm{r}\left(\nabla\bullet\vec{W}\right) -2\nabla\times\left(\omega\times\vec{W}\right)+\frac{\nabla\rho_\mathrm{m}\times\nabla p}{\rho_\mathrm{m}^2}+\nu\nabla^2\Omega_\mathrm{r} \quad (9)$$

where Ω_r is the relative vorticity, $\vec{W}$ is the relative velocity, and ν is the kinematic viscosity.

In Eq. (9), the term on the Left-hand side (LHS) is the rate of vorticity change that results from fluid convection. For the Right-hand side (RHS), the first term is a relative vortex stretching that is attributed to velocity gradients. The second term on RHS is the relative vortex dilation that results from relative velocity divergences, which demonstrates the effects of fluid compressibility on relative vorticity. The third term on RHS represents the effects of the Coriolis force, which influences relative vorticity in the rotational frame. The fourth term on RHS originates from baroclinic torque and reaches zero in barotropic fluids. The last term on RHS demonstrates that viscous diffusion can result in the rate of change in relative vorticity.

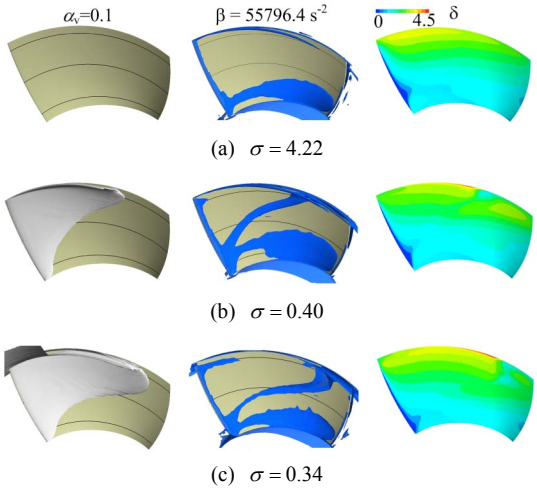

Fig. 6. 3D view of vapor volume fraction isosurface α_v = 0.1 (left), relative vorticity with Q-criterion β of 55796.4 s^{-2} (middle), and turbulent kinetic energy δ distribution (right).

To visualize the effects of cavitation on vortex generation around the impeller vane, the calculated results are illustrated on the suction side in Fig. 6, along with the plotting vapor of volume fraction α_v = 0.1, vorticity isosurface of Q-criterion β = 55796.4 s^{-2}, and turbulent kinetic energy δ at three cavitation numbers (σ = 4.22, 0.40, and 0.34). Flow features were clearly observed along the suction side. (1) No cavity was found inside the impeller at non-cavitation condition (σ = 4.22). Compared with that in Fig. 6(left), cavities are likely to generate at the vane tip and then grow downstream along the vane suction side as cavitation develops.

(2) Vortices were initially located on the suction side near the hub and then rose as cavitation developed, particularly at the downstream cavities indicated in Fig. 6(middle). (3) Large vortices could be observed at the vapor-liquid interface σ = 0.34 than that at σ = 0.40. Turbulent kinetic energy exhibited an upward trend along with cavitation development, which indicated that turbulent unsteadiness and vortices could be aggravated by the transition from sheet cavitation to cloud cavitation, as demonstrated by Foeth et al. [25]. Therefore, cavitation promotes vorticity generation and flow unsteadiness in the mixed-flow waterjet pump. Vortices are basically located at the cavity interface, particularly the downstream interface during the process of cavitation development.

To investigate cavitation-vortex interaction in the impeller further, cavitation contours, vorticity, and all terms on RHS in Eq. (9) were shown along a typical span section of 0.9 at three cavitation stages (σ = 4.22, 0.40, and 0.34). Note that span = 0.9 plane was near the impeller shroud and span = 0.1 plane was near the hub. Fig. 7 shows the vapor and relative vorticity

Table 3. Hydraulic characteristics at three cavitation stages (Q = 0.445 m^3/s, n = 1450 r/min).

σ	Ψ	η
4.22	0.3485	89.58%
0.40	0.3481	89.02%
0.34	0.3397	85.87%

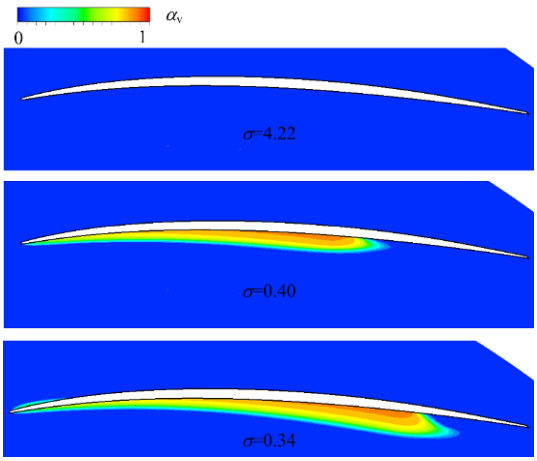

(a) Vapor volume fraction at span = 0.9

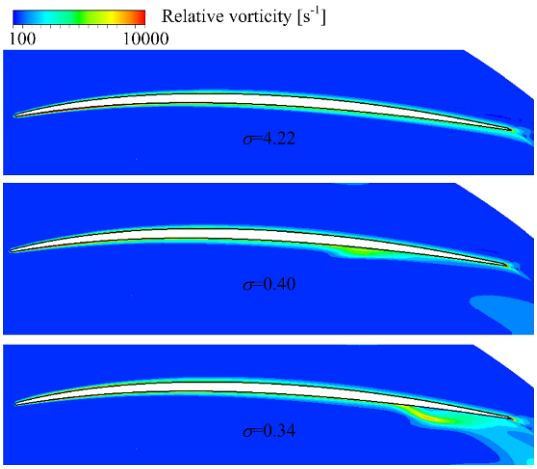

(b) Relative vorticity at span = 0.9

Fig. 7. Comparison of vapor volume fraction (a); and relative vorticity (b) contours at span = 0.9 plane.

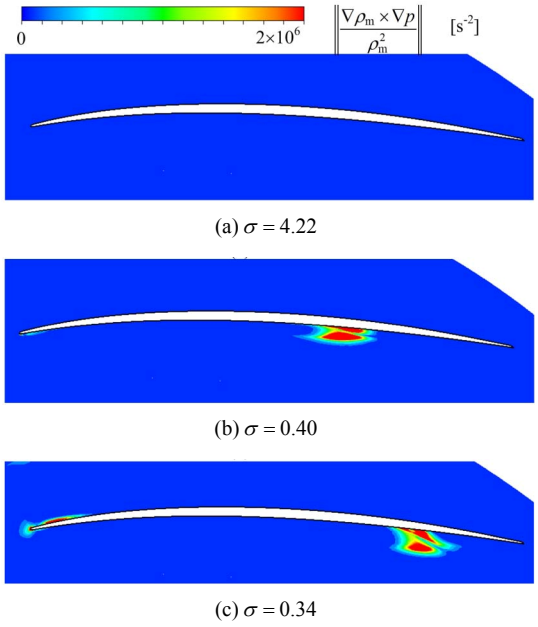

(a) σ = 4.22

(b) σ = 0.40

(c) σ = 0.34

Fig. 8. Comparison of baroclinic torque contours at span = 0.9 plane.

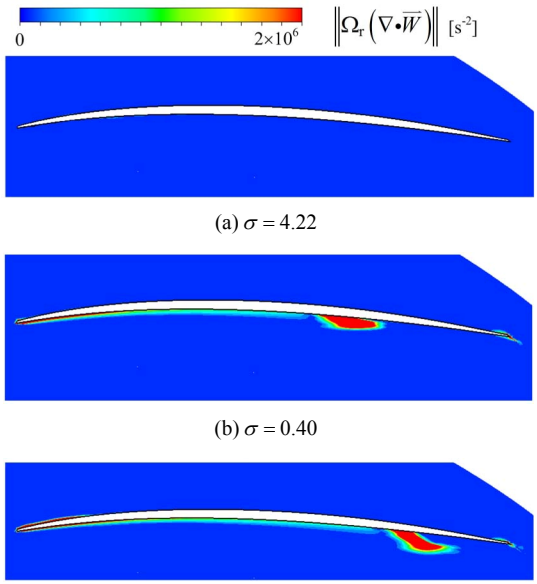

(a) σ = 4.22

(b) σ = 0.40

(c) σ = 0.34

Fig. 9. Comparison of vortex dilation contours at span = 0.9 plane.

contours at span = 0.9 plane, which demonstrates that vapor cavity length and vorticity intensity increase with cavitation development. Cavities were then detached from the rear vane surface, which could result in vortices shedding the downstream fluids indicated in Fig. 6. Hydraulic characteristics such as head coefficients and hydraulic efficiency decreased with vortex-cavitation interaction, as listed in Table 3.

Figs. 8-12 clearly indicate that a baroclinic torque term is important for vortex generation during cavitation development because density gradients are not in parallel with pressure gradients in cavitating fluids. Note that the baroclinic torque term mainly focused on the downstream cavity interface shown in Fig. 8. Although the baroclinic torque term has significant effects on cavitation, the main contributor to vortex generation is the vortex dilation term, whose magnitude appears to be larger when compared with the baroclinic torque term. The vortex dilation term, in proportion to relative velocity divergence $\nabla\bullet\vec{W}$, is zero in non-cavitating flows but plays a dominant role in cavitating flows because cavitation may aggravate the mass transfer process according to the simulated work by Ji et al. [26].

Moreover, vortex stretching, the Coriolis force, and viscous diffusion are visible under non-cavitation condition (σ= 4.22),

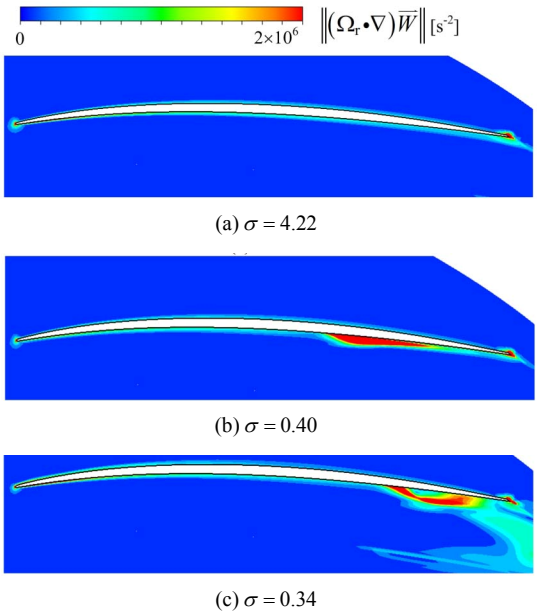

Fig. 10. Comparison of vortex stretching contours at span = 0.9 plane.

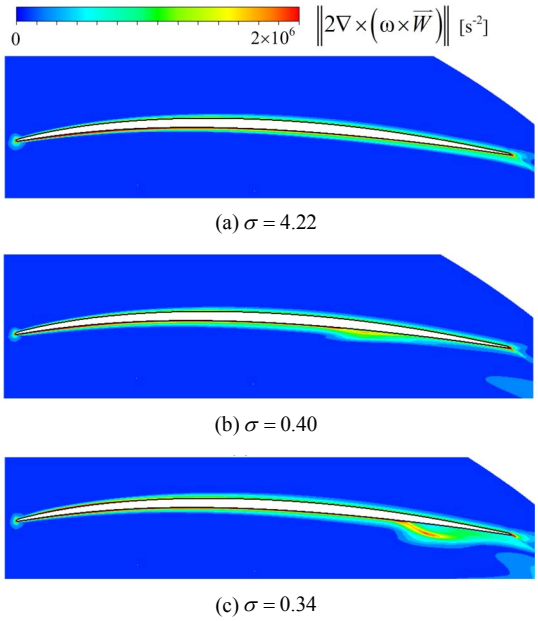

Fig. 11. Comparison of the Coriolis force contours at span = 0.9 plane.

as shown in Figs. 10-12, respectively. A magnitude jump, particularly near the vapor-liquid interface, was observed as cavitation occurred. Although the effects of the Coriolis force should be considered in rotational fluid machines, vortex stretching and viscous diffusion terms are significant in large-scale vortex generation during cavitation diffusion, with vortex stretching as the main contributor. According to the vortex dynamics illustrated by Wu et al. [27], vortex stretching would weaken the moment of inertia in fluids, increase angular momentum, and promote the production of a large-scale vortex, which confirms that the vortex stretching term has the largest

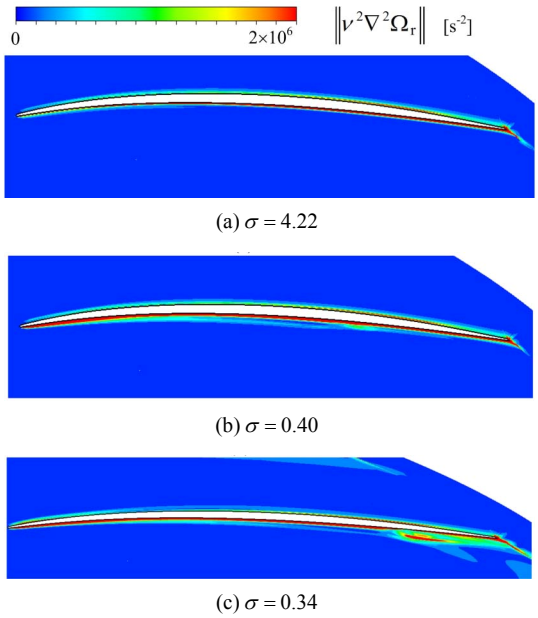

Fig. 12. Comparison of viscous diffusion contours at span = 0.9 plane.

magnitude compared with the Coriolis force and viscous diffusion terms.

Fig. 13 presents vapor volume fraction distribution (σ = 0.34) along with baroclinic torque, vortex dilation, and vortex stretching contours at three span surfaces. As demonstrated, cavity became increasingly long when the span plane was far from the hub and near the rear part of the impeller vane at span = 0.9 plane. Meanwhile, the baroclinic torque, vortex dilation, and stretching term shown in Figs. 14-16 moved downstream along with the increase in the span plane. The high-value region, which was concentrated on the downstream interface, was obviously visible at the span = 0.9 plane because cavities might become increasingly large and unstable given the fluctuating and shedding into cloud cavitation, which would cause vorticity production and flow unsteadiness.

5. Conclusions

Cavitating turbulent flows in a mixed-flow waterjet pump were simulated using the *k*-ω SST turbulence model and the mass transfer cavitation model based on the Rayleigh-Plesset equation. The following conclusions can be drawn from the present investigation.

(1) The calculated characteristics (i.e., pump head coefficient and hydraulic efficiency) and the effects of cavitation on pump performance predicted by the present numerical method fit reasonably well with the experimental results.

(2) Cavitation development remarkably enhances vortex generation and flow unsteadiness in the mixed-flow waterjet pump. Furthermore, the vortices are basically located at the cavity interface, particularly the downstream interface, during cavitation.

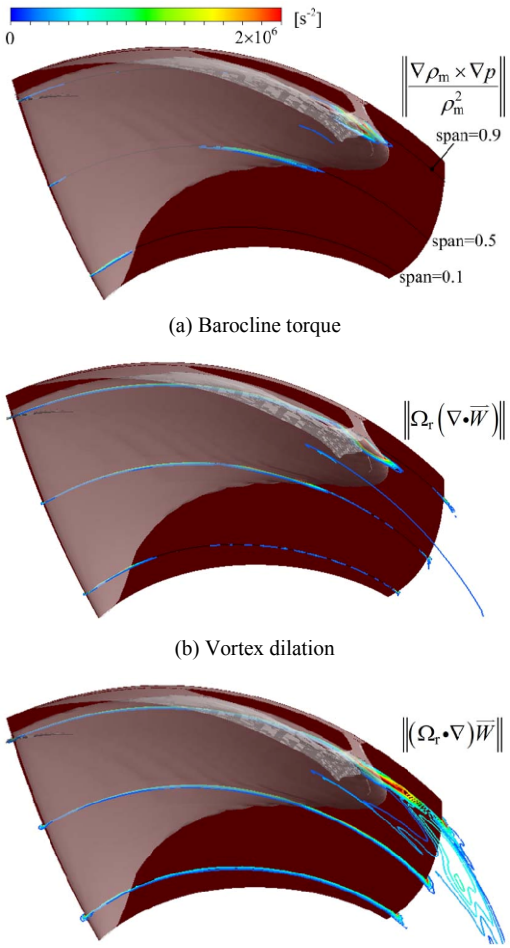

(a) Barocline torque

(b) Vortex dilation

(c) Vortex stretching

Fig. 13. 3D view of the vapor volume fraction isosurface of α_v = 0.1 with baroclinic torque, vortex dilation, and vortex stretching contours at σ = 0.34.

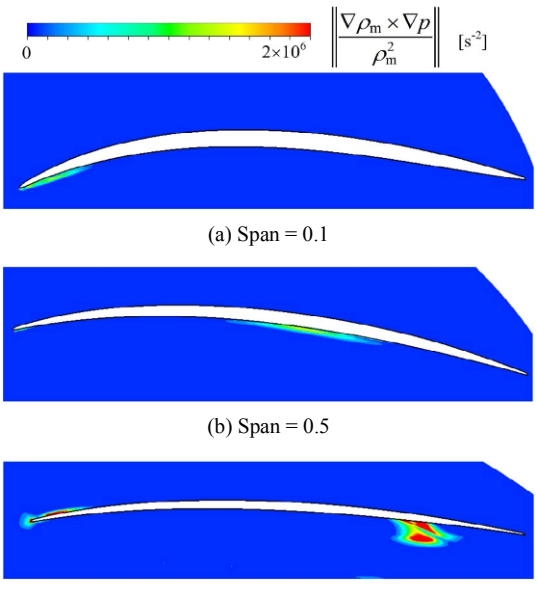

(a) Span = 0.1

(b) Span = 0.5

(c) Span = 0.9

Fig. 14. Comparison of baroclinic torque contours for σ = 0.34.

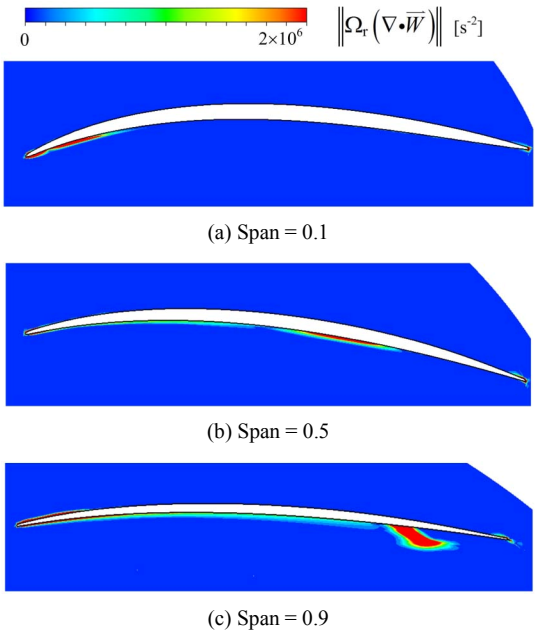

(a) Span = 0.1

(b) Span = 0.5

(c) Span = 0.9

Fig. 15. Comparison of vortex dilation contours for σ = 0.34.

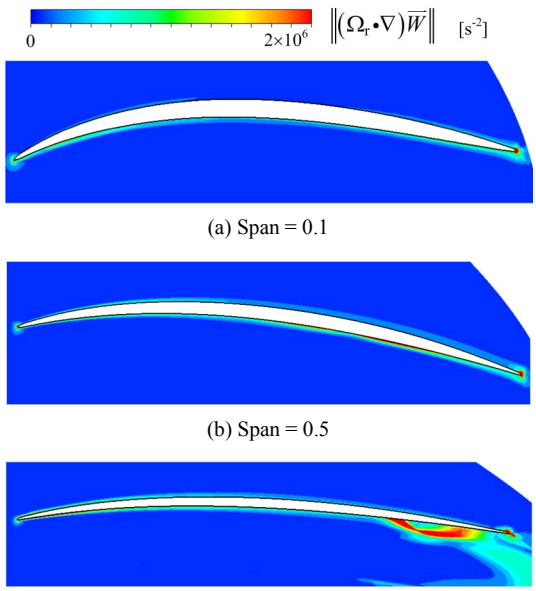

(a) Span = 0.1

(b) Span = 0.5

(c) Span = 0.9

Fig. 16. Comparison of vortex stretching contours for σ = 0.34.

(3) Analyses based on the relative vorticity transport equation indicate that the vortex dilation and baroclinic torque of turbulent flows dramatically increase at the cavity interface as cavitation occurs, and the vortex dilation term has a larger magnitude than the baroclinic torque. Although the effects of the Coriolis force should be considered in rotational fluid machines, vortex stretching and viscous diffusion terms are significant for large-scale vortex generation during cavitation diffusion with vortex stretching as the main contributor.

Acknowledgment

This work was financially supported by the National Natural Science Foundation of China (Project Nos. 51376100, 51206087, 51306018, and 51179091), the National Key Technology Research and Development Program (Grant No. 2011BAF03B01), and the State Key Laboratory for Hydroscience and Engineering (Project Nos. 2014-KY-05 and 2015-E-03).

Nomenclature

b_1 : Blade width at the impeller inlet
b_2 : Blade width at the impeller outlet
D_{1h} : Blade hub diameter at the impeller inlet
D_{1t} : Blade tip diameter at the impeller inlet
D_2 : Blade tip diameter at the impeller outlet
F_{vap} : Empirical coefficients for the mass transfer process
F_{cond} : Empirical coefficients for the mass transfer process
g : Gravity acceleration
H : Pump head
l : Subscript that represents liquid phase
$\dot{m}^+$: Vaporization term
$\dot{m}^-$: Condensation term
M : Torque input to pump shaft
n : Rotational speed = 1450 r/min
$NPSH_A$: Available net positive suction head
p : Mixture pressure
p_{in} : Static pressure at the inlet plane
p_v : Saturation vapor pressure of water at 25 °C
Q : Flow discharge
r_{nuc} : Nucleation volume fraction = 5×10^{-4}
R_{nuc} : Bubble radius = 1×10^{-6} m
u_i : Velocity in the i direction
u_2 : Peripheral velocity at the exit of the blade tip = $\omega D_2/2$
v : Subscript that represents vapor phase
v_{in} : Velocity at the inlet plane
$\overline{W}$: Relative velocity
α_v : Vapor volume fraction
β : Relative vorticity with Q-criterion
δ : Turbulent kinetic energy
η : Hydraulic efficiency, as listed in Table 2
μ : Laminar viscosity
μ_t : Turbulent eddy viscosity
ν : Kinematic viscosity
ρ_m : Mixture density
σ : Thoma's cavitation number = $NPSH_A/H$
ϕ : Flow coefficient, as listed in Table 2
Ψ : Head coefficient, as listed in Table 2
Ω : Rotational angular velocity = $2\pi n/60$
Ω_r : Relative vorticity

References

[1] H. W. Oh, E. S. Yoon, K. S. Kim and J. W. Ahn, A practical approach to the hydraulic design and performance analysis of a mixed-flow pump for marine waterjet propulsion, *Proceedings of the Institution of Mechanical Engineers, Part A: Journal of Power and Energy*, 217 (6) (2003) 659-664.

[2] H. W. Oh and E. S. Yoon, Hydrodynamically detailed performance analysis of a mixed-flow waterjet pump using computational fluid dynamics, *Proceedings of the Institution of Mechanical Engineers, Part C: Journal of Mechanical Engineering Science*, 222 (9) (2008) 1861-1867.

[3] H. W. Oh, Design parameter to improve the suction performance of mixed-flow pump impeller, *Proceedings of the Institution of Mechanical Engineers, Part A: Journal of Power and Energy*, 224 (6) (2010) 881-887.

[4] D. Bonaiuti, M. Zangeneh, R. Aartojarvi and J. Eriksson, Parametric design of a waterjet pump by means of inverse design, CFD calculations and experimental analyses, *Journal of Fluids Engineering*, 132 (3) (2010) 0311041-03110415.

[5] X. Luo, B. Ji and H. Xu, *Design and optimization for fluid machinery*, Tsinghua University, Beijing, China (2012).

[6] X. Luo, W. Wei, B. Ji, Z. Pan, W. Zhou and H. Xu, Comparison of cavitation prediction for a centrifugal pump with or without volute casing, *Journal of Mechanical Science and Technology*, 27 (6) (2013) 1643-1648.

[7] Y. Wu, J. Liu, Y. Sun, S. Liu and Z. Zuo, Numerical analysis of flow in a Francis turbine on an equal critical cavitation coefficient line, *Journal of Mechanical Science and Technology*, 27 (6) (2013) 1635-1641.

[8] B. Ji, X. Luo, Y. Wu, X. Peng and Y. Duan, Numerical analysis of unsteady cavitating turbulent flow and shedding horse-shoe vortex structure around a twisted hydrofoil, *International Journal of Multiphase Flow*, 51 (2013) 33-43.

[9] X. Tang, L. Bian, F. Wang, X. Li and M. Hao, Numerical investigations on cavitating flows with thermodynamic effects in a diffuser-type centrifugal pump, *Journal of Mechanical Science and Technology*, 27 (6) (2013) 1655-1664.

[10] H. Liu, Y. Wang, D. Liu, S. Yuan and J. Wang, Assessment of the turbulence model for numerical predictions of sheet-cavitating flows in centrifugal pumps, *Journal of Mechanical Science and Technology*, 27 (9) (2013) 2743-2750.

[11] X. Zhang, Z. Wu, S. Xiang and L. Qiu, Modeling cavitation flow of cryogenic fluids with thermodynamic phase-change theory, *Chinese Science Bulletin*, 58 (4-5) (2013) 567-574.

[12] T. Watanabe, T. Kawamura, Y. Takekoshi, M. Maeda and S. H. Rhee, Simulation of steady and unsteady cavitation on a marine propeller using a RANS CFD code, *Proc. of the Fifth International Symposium on Cavitation*, Osaka, Japan (2003).

[13] B. Ji, X. Luo, R. Arndt, X. Peng and Y. Wu, Large Eddy Simulation and theoretical investigations of the transient cavitating vortical flow structure around a NACA66 hydrofoil, *International Journal of Multiphase Flow*, 68 (2015) 121-134.

[14] S. A. Kinnas, H. Lee, T. J. Michael and H. Sun, Prediction of cavitating waterjet propulsor performance using a boundary element method, *Proc. of 9th International Conference*

on Numerical Ship Hydrodynamics, Ann Arbor, USA (2007).

[15] H. Wu, F. Soranna, T. Michael, J. Katz and S. Jessup, Cavitation visualizes the flow structure in the tip region of a waterjet pump rotor blade, *Proc. of 27th Symposium on Naval Hydrodynamics*, Seoul, Korea (2008).

[16] J. W. Lindau, W. L. Moody, M. P. Kinzel, J. J. Dreyer, R. F. Kunz and E. G. Paterson, Computation of cavitating flow through marine propulsors, *Proc. of First Internation- al Symposium on Marine Propulsors*, Trondheim, Norway (2009) 1-10.

[17] S. Schroeder, S. E. Kim and H. Jasak, Toward predicting performance of an axial flow waterjet including the effects of cavitation and thrust breakdown, *Proc. of First International Symposium on Marine Propulsors*, Trondheim, Norway (2009).

[18] S. H. Rhee, T. Kawamura and H. Li, Propeller cavitation study using an unstructured grid based Navier-Stoker solver, *Journal of Fluids Engineering*, 127 (5) (2005) 986-994.

[19] R. E. A. Arndt, Cavitation in vortical flows, *Annual Review of Fluid Mechanics*, 34 (1) (2002) 143-175.

[20] J. Choi, C. T. Hsiao, G. Chahine and S. Ceccio, Growth, oscillation and collapse of vortex cavitation bubbles, *Journal of Fluid Mechanics*, 624 (2009) 255-279.

[21] J. Bardina, P. Huang and T. Coakley, Turbulence modeling validation, *AIAA paper*, 2121 (1997).

[22] P. J. Zwart, A. G. Gerber and T. Belamri, A two-phase flow model for predicting cavitation dynamics, *Proc. of the Fifth International Conference on Multiphase Flow*, Yokohama, Japan (2004).

[23] C. C. Tseng and L. J. Wang, Investigations of empirical coefficients of cavitation and turbulence model through steady and unsteady turbulent cavitating flows, *Computers & Fluids*, 103 (2014) 262-274.

[24] L. Zhou and Z. Wang, Numerical simulation of cavitation around a hydrofoil and evaluation of a RNG κ-ε model, *Journal of Fluids Engineering*, 130 (1) (2008) 011302.

[25] E. J. Foeth, T. van Terwisga and C. van Doorne, On the collapse structure of an attached cavity on a three-dimensional hydrofoil, *Journal of Fluids Engineering*, 130 (7) (2008) 071303.

[26] B. Ji, X. Luo, R. E. Arndt and Y. Wu, Numerical simulation of three dimensional cavitation shedding dynamics with special emphasis on cavitation-vortex interaction, *Ocean Engineering*, 87 (2014) 64-77.

[27] J. Wu, H. Ma and M. Zhou, *Vorticity and vortex dynamics*, Springer Berlin Heidelberg (2006).

Xianwu Luo obtained his B.S. and M.S. degrees from Tsinghua University, Beijing, China in 1991 and 1997, respectively, and his Ph.D. in Mechanical Engineering from Kyushu Institute of Technology, Japan, in 2004. He is currently an associate professor at the Department of Thermal Engineering, Tsinghua University, China.